Chinese Chemical Letters 37 (2026) 112042

Contents lists available at ScienceDirect

Chinese Chemical Letters

journal homepage: www.elsevier.com/locate/cclet

Ion-equilibrated OECT inverters for neural-compatible ring oscillators

Xiangyuan Mei[a,b], Yu Xiao[b,c], Chaoyi Yan[b], Lingxuan Jia[a], Gang Song[a], Runjie Zhang[b], Weijie Wang[a], Fengting Lv[a], Xiaojuan Dai[a], Liyao Liu[a], Ye Zou[a], Shu Wang[a], Chong-an Di[a,*], Daoben Zhu[a], Fengjiao Zhang[b,c,*]

[a] Beijing National Laboratory for Molecular Sciences, CAS Key Laboratory of Organic Solids, Institute of Chemistry, Chinese Academy of Sciences, Beijing 100190, China
[b] School of Chemical Sciences, University of Chinese Academy of Sciences, Beijing 101408, China
[c] Binzhou Institute of Technology, Binzhou 256606, China

ARTICLE INFO

Article history:
Received 5 August 2025
Revised 24 October 2025
Accepted 30 October 2025
Available online 30 October 2025

Keywords:
Organic electrochemical transistors
Complementary inverter
Ring oscillator
Ion concentration
Neural transconductance

ABSTRACT

Organic electrochemical transistor (OECT)-based inverters hold great promise for neural-machine interfaces due to their low operating voltage and compatibility with aqueous environments. However, unbalanced p-/n-channel characteristics hinder the inverter's voltage gain and fast switching. Here, a rational inverter design is presented, leveraging ion concentration to equilibrate p-n channel conductivity and kinetic doping in the OECT inverter, achieving an extremely high gain value of over 370 V/V under optimized driving conditions. Furthermore, a 3-stage ring oscillator constructed from these ion-equilibrated OECT inverters exhibits a rapid response time (stage delay < 0.6 ms) and a broad frequency response exceeding 300 Hz, matching the mechanoreceptor signals in human skin. The biocompatible output displays a sublinear reaction to static pressure pulses, indicating successful tactile recognition in live neurons. This work presents a practical strategy for constructing neural-compatible artificial logics through ion-concentration engineering, providing a platform for seamless neural-machine integration.

© 2025 Published by Elsevier B.V. on behalf of Chinese Chemical Society and Institute of Materia Medica, Chinese Academy of Medical Sciences.

Artificial afferent nerves aim to efficiently encode physical chemistry or mechanical stimuli into biocompatible signals. Organic electrochemical transistors (OECTs), which exhibit high transconductance and aqueous compatibility [1,2], rely on the injection/extraction of ions from electrolyte, have emerged as key building blocks for bioelectronic interfaces [3–7] and neuromorphic circuits [8–12]. With the development of p- and n-type organic mixed ionic–electronic conductors (OMIECs), OECT-based complementary inverters have been of great interest for researchers, which can directly output voltage signals to interfacing sensory receptors and afferent neurons without the need for current-to-voltage conversion [13–15]. However, translating static electronic signals into dynamic ionic signals, which is critical for neural compatibility, requires OECT-based inverters capable of operating at biological frequencies (0.3–500 Hz) [16,17]. Existing OECT inverters, especially in the context of a ring oscillator, struggle to match the temporal fidelity of neural signals, primarily due to the challenge in balance and dynamics of ion-gated electron and hole transport in both p- and n- channels, resulting in delayed doping/de-doping cycles and limited switching speeds.

Over the past decades, the performance of OECT-based inverters has improved significantly. Higher gain enables faster signal transitions by minimizing propagation delay in organic inverter–based ring oscillators, thereby achieving higher oscillation frequencies suitable for biomimetic applications [18–20]. To date, conventional strategies have focused on developing novel n-type OMIECs or ambipolar materials to achieve temporal and operational alignment of ion dynamics. This alignment is essential for rapid and balanced electrochemical doping and de-doping in both p- and n-type channels, ultimately enhancing conductivity modulation and switching speeds in complementary circuits [21–24]. For instance, Stein *et al.* introduced ambipolar blend OECTs based on $PrC_{6n}MA$:p(g2T-TT), offering a simple and tunable route to high-gain inverters (82 V/V at $V_{DD} = 0.9$ V) [25]. In 2025, Ge *et al.* demonstrated a high-spin polymer P(TII-2FT) with balanced ambipolar OECT performance by utilizing the singlet-triplet energy gap (ΔE_{ST}) to select the comonomer for materials design, which brings a high gain of 809 V/V at a voltage step size of 0.1 mV and a V_{DD} of 0.8 V [26]. Recent studies have demonstrated that rationally designing the architecture of inverter devices is an effective approach to synergistically modulate ion-gated electron and hole transport [27]. Hung *et al.* further advanced the complementary OECTs by introducing vertical geometry using Cin-Cell blended gDPP-g2T (p-type) and

* Corresponding authors.
E-mail addresses: dicha@iccas.ac.cn (C. Di), fjiaozhang@ucas.ac.cn (F. Zhang).

https://doi.org/10.1016/j.cclet.2025.112042
1001-8417/© 2025 Published by Elsevier B.V. on behalf of Chinese Chemical Society and Institute of Materia Medica, Chinese Academy of Medical Sciences.

Homo-gDPP (n-type) [13]. The complementary vertical OECT logic circuits, with effectively ion drift velocity along the short channel length, exhibited fast doping for a high gain of 150 V/V at V_{DD} of 0.7 V. More recently, Wang *et al.* proposed a high-performance vertical-OECT incorporating a gradient-intermixed biocontinuous structure from BBL and PEI dopants, establishing separate ionic and electronic transport pathways [28]. This approach enhanced both ion storage and charge transport in n-channel OECT, enabling an amplifier based on BBL/PEI and PTBT-P to achieve a gain of ~250 V/V under $V_{DD} = 0.8$ V. These advancements enabled the construction of axon-hillock circuits for frequency-encoded spiking neuron emulation. Although these strategies have effectively facilitated dynamic ion regulation within OMIECs, thereby reducing the mismatch conductance switch in OECT performance, challenges persist in simplified dynamic parallelism in ion doping across two channels.

The operation of an OECT device is fundamentally governed by ion-mediated electrochemical doping and de-doping. Based on this, Romele *et al.* demonstrated that the ion concentration can modulate the transition voltage V_M of an OECT-inverter, enabling the multiscale, real-time, and high-sensitivity ion detection [29,30]. This concept also inspired the development of organic electrochemical neurons by manipulating the stable, ion-tunable antiambipolar behavior [9]. Motivated by these advances, we introduce a simple ion-equilibration strategy that enables systematic manipulation of the doping kinetics in complementary OECT inverters with high electrical performance. By integrating poly(2-(3,3′-bis(2-(2-(2-methoxyethoxy)ethoxy)ethoxy)-[2,2′-bithiophen]−5-yl)thieno[3,2-*b*] thiophene) (p(g2T-TT)) and PNDI2TEG-2Tz (N2200–2B) [31] channels within a shared electrolyte, treated with distinct ion concentrations, we achieve tailored electrical responses that compensate for intrinsic material disparities. This approach achieves balanced switching dynamics, yielding a 5-fold enhancement in switching speed and a record gain value of 371.7 V/V at $V_{DD} = 0.7$ V. Leveraging this inverter, we fabricate a 3-stage ring oscillator with a frequency modulation covering three orders of magnitude from 0.1 Hz to >300 Hz, compatible with human tactile recognition. The system successfully interfaces commercial pressure sensors with neuronal circuits, triggering synchronous action potentials. This approach highlights the importance of electrolyte engineering in synchronizing ionic responses and advancing robust, neural-compatible bioelectronic platforms.

We first conducted a comprehensive evaluation of the performance of the complementary OECT-based inverters. As shown in Fig. 1a, the complementary inverter consists of p(g2T-TT) and N2200–2B as the p- and n-type channels, respectively, integrated on the same electrolyte (Figs. S1, S2, and details provided in Methods section in Supporting information). Both the p- and n-type channels exhibited representative characteristic OECT behavior (Figs. 1b and c). Notably, relatively comparable ON currents were achieved for two types of OECTs ($I_{on,p} = -0.43$ mA, $I_{on,n} = 0.15$ mA) along with low OFF currents ($I_{off} < 10^{-7}$ A), owing to an optimized device geometry (W_n:W_p = 10:1) and the use of 150 mmol/L PBS electrolyte. The peak transconductances were measured as $g_{m,p} = 1.68 \pm 0.01$ mS for the p-type OECT and $g_{m,n} = 0.74 \pm 0.02$ mS for the n-type OECT under the same electrolyte conditions. These results indicate that the use of p(g2T-TT) and N2200–2B as OMIECs enables ion penetration and well-regulated redox doping processes. We further assessed the dynamic performance of these devices under pulsed V_{GS} switching. After 1000 alternating cycles at a switching frequency of 1 Hz, both p- and n-type OECTs maintained stable ON/OFF current ratios of approximately 10^4, with no significant current degradation observed (Fig. 1d). Additionally, corresponding transient on-state response of p(g2T-TT) and N2200–2B OECTs were assessed as 6.95 ms and 8.51 ms, while off-state

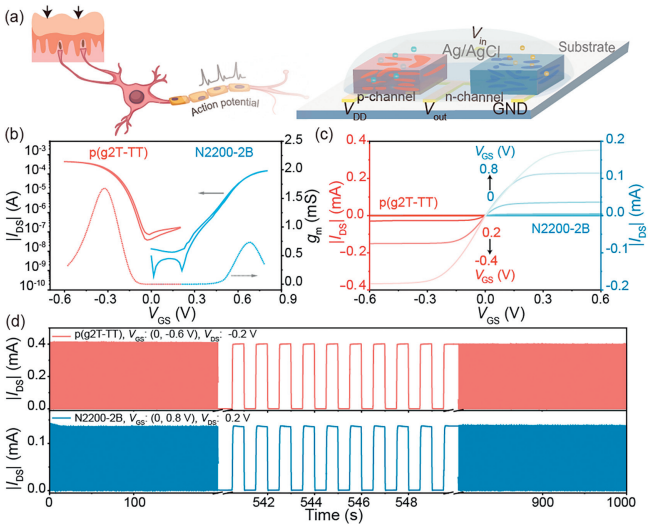


Fig. 1. (a) Signal transduction mode of the tactile afferent nerve (left) and schematic of OECT-based complementary inverter (right). p-OECT and n-OECT were fabricated with p(g2T-TT) and N2200–2B with a shared liquid electrolyte, and an Ag/AgCl electrode was used as the gate. Transfer curves (b) and output curves (c) of p(g2T-TT) and N2200–2B-based OECTs. The transfer curves were operated at $V_{DS} = -0.2$ V (p-channel, red) and $V_{DS} = +0.2$ V (n-channel, blue), respectively. A channel length of 5 μm was used for both p- and n-type OECTs, while n-channel width is 10 times for p-channel ($W_p = 150$ μm, $W_n = 1500$ μm). The electrolyte solution is 150 mmol/L PBS. (d) Cycling stability of p-type and n-type OECTs, where $V_{DS} = -0.2$ V, V_{GS} is switching between 0 and −0.6 V for the p-type device, and $V_{DS} = +0.2$ V, V_G is switching between 0 and +0.8 V for the n-type device.

response time is 5.27 ms and 6.31 ms (Fig. S3 in Supporting information), respectively, when $V_{DS} = -0.2$ V for the p-type and $V_{DS} = 0.2$ V for the n-type, indicating p- and n-type OECTs have the potential for high-gain complementary inverter applications with long-term operational stability.

Having demonstrated the long-term stability and ion penetration quality of p(g2T-TT) and N2200–2B channels, we then proceeded to fine-tune the electrical performance of the complementary inverter by systematically varying the electrolyte ion concentration from 1.0 mmol/L PBS to 300 mmol/L PBS. In this context, the switching resistance of the inverter is expected to depend on the selective and synchronous penetration of cations and anions within the electrolyte. As illustrated in Figs. 2a and b, and Fig. S4 (Supporting information), the transfer curves and output curves of both p(g2T-TT) and N2200–2B channel negatively shift when increasing the PBS concentration. Specifically, the channel current and transconductance of p-type OECTs decreased, while that of n-type OECTs almost increased as the PBS concentration increased. Meanwhile, the threshold voltage (V_{TH}) of the p-type device shifted from –0.04 V to –0.27 V, while the n-type device shifted from 0.68 V to 0.32 V (Fig. 2c). In parallel, the gating efficiency, characterized by the saturation drain current (I_{DSAT}) of the p-type channel, $|I_{DSAT,\,p}|$, monotonically decreased from 0.37 mA to 0.13 mA as the ion concentration increased. Interestingly, the n-type channel showed a non-monotonic trend: $I_{DSAT,n}$ initially increased from ~0.01 mA to 0.16 mA with increasing the electrolyte from 1.0 mmol/L PBS to 150 mmol/L PBS, followed by a gradual decrease to 0.12 mA at 300 mmol/L PBS. These results highlight that precise tuning of ion concentration can effectively achieve balanced driving strengths of the pull-up and pull-down transistors between p-type and n-type channels, thereby enabling faster and more efficient logic circuit inversion. Notably, this modulation strategy also leads to a reduction in the operation voltage required to achieve ion storage saturation, supporting lower power consumption and faster switching behavior (Fig. 2d).

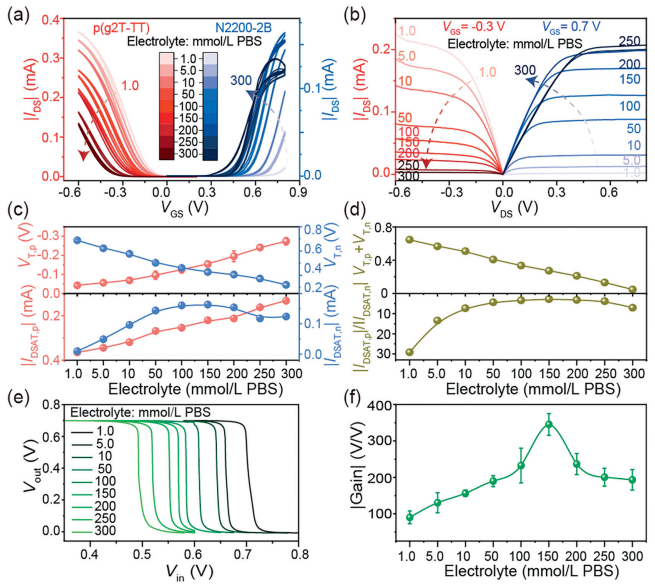


Fig. 2. (a) Ion concentration-dependent transfer curves of p-type OECT (red line, $V_{DS} = -0.2$ V) and n-type OECT (blue line, $V_{DS} = 0.2$ V). Dashed arrows label the transfer curve shift from low to high PBS concentration. (b) Output curves of p-type OECT in red line ($V_{GS} = -0.3$ V, V_{DS} scanning from 0 V to −0.6 V), and for n-type OECT in blue line ($V_{GS} = 0.7$ V and scanning V_{DS} from 0 V to 0.8 V). Dashed arrows label the output curve changes from low to high PBS concentration. (c) Extracted threshold voltage and saturation currents of p-and n-type OECT, as a function of electrolyte ion concentration. (d) Ion concentration-dependent $V_{T,n} + V_{T,p}$, and ratio of $I_{DSAT,p}/I_{DSAT,n}$. Typical voltage transfer characteristics (VTC) (e) and statistical peak gains (f) of the inverters at various supply voltages under different electrolytes. V_{in} changed from 0.3 V to 0.8 V with constant $V_{DD} = 0.7$ V.

Furthermore, the ion concentration-dependent electrochemical performance of the inverter was systematically investigated. Here, the inverter pulls up when the p(g2T-TT)-based transistor switches on to off in response to a gradual change in gate voltage (V_{in}) between 0.3 V and 0.8 V, while the pull-down is dependent on the N2200–2B-based transistor works oppositely. The fabricated inverter achieved full rail-to-rail swing from GND to V_{DD} with a sharp transition curve due to the low OFF current in p- and n-type devices (Fig. 2e and Fig. S5 in Supporting information). In addition, the maximum gain value of 371.7 V/V at $V_{DD} = 0.7$ V was achieved at the transition peak with gradually increasing PBS concentration from 1.0 mmol/L to 150 mmol/L, providing a good potential in touch signal transmission with human (Fig. 2f). More importantly, the gain value obtained by fine-tuned electrolyte ion concentration is among the best reported OECT integrated technologies (Table S1 in Supporting information). This excellent result can be attributed to the well-balanced p-/n-channel's electrical characteristics of p- and n-type transistors in complementary inverters. Moreover, the inverter operation at 150 mmol/L PBS exhibited voltage gain over 200 V/V even at low $V_{DD} = 0.5$ V with a V_M of 0.46 V, the static power consumption of 1.07 μW, and dynamic power consumption of 10.3 μW (Figs. S6 and S7 in Supporting information). Interestingly, similar phenomena can be achieved when devices are operated in different NaCl solutions (Fig. S8 in Supporting information), indicating that ion concentration effects on electrical performance modulation, and 150 mmol/L NaCl is also the best electrolyte concentration for high gain OECT inverter.

In general, a higher ion concentration facilitates bulk doping by enhancing ion penetration, which typically lowers the energy barrier for charge injection. However, excessive ion infiltration can also interfere with π–π stacking pathways, potentially disrupting efficient charge transport. To reveal how the concentration of electrolyte ions regulates the performance of such inverters, we systematically investigated the effects of ions on the redox behavior and charge transport of p- and n-type OMIECs. We performed spectroelectrochemistry measurements to explore how the ion concentration affects the doping speed and electronic structure (doping level) upon electrochemical doping in PBS aqueous electrolyte with different concentrations (Fig. S9 in Supporting information). Principally, higher ion concentration increases the ionic conductivity of the electrolyte, enabling faster ion migration and thus accelerating electrochemical doping/dedoping of the channel; and higher ion concentration enhances the interfacial capacitance, resulting in larger voltage drops across the channel/electrolyte interface, which lowers the ion injection barrier and promotes more efficient electrochemical reactions. As shown in Fig. 3a, Figs. S10 and S11 (Supporting information), p(g2T-TT) films undergo efficient electrochemical doping at low bias (−0.6 V *vs.* Ag/AgCl), evidenced by the bleaching ground-state π–π^* absorption (~600 nm) and the emergence of a broad polaron band around 900 nm. These spectral changes indicate anion insertion from the electrolyte into the polymer bulk, facilitating charge carrier accumulation. With increasing electrolyte concentration, the temporal evolution of the absorption features accelerates, with the characteristic doping time constant (τ) decreasing from 0.15 s to 0.05 s, reflecting half an order-of-magnitude enhancement in oxidation kinetics. In contrast, N2200–2B films exhibit sluggish electrochemical doping at low ionic strength, attributed to a significant ion injection barrier. However, above a threshold of 50 mmol/L PBS, a pronounced increase in optical density is observed, indicating improved doping efficiency. Correspondingly, the reduction time constant τ decreases from 0.36 s to 0.05 s as the electrolyte concentration increases (Fig. S12 in Supporting information). The decreasing trend in τ for both p- and n-type channels with increasing ion concentration (1.0 mmol/L to 150 mmol/L PBS) aligns with the observed reduction in threshold voltage (V_{TH}) in their respective transfer characteristics. This enhanced ionic concentration contributes directly to the rapid pull-up and pull-down transitions of the inverter under voltage input, supporting high-speed signal switching performance.

Grazing-incidence wide-angle X-ray scattering (GIWAXS) was conducted to evaluate the influence of electrolyte ions on the molecular packing of p(g2T-TT) and N2200–2B films. As shown in Fig. S13 (Supporting information), both pristine films exhibit well-defined semicrystalline features and slightly change during swelling. These structural changes, corroborated by polarized absorption data (Fig. 3b and Fig. S14 in Supporting information), reveal two key phenomena: (1) Elevated ion concentrations facilitate higher doping levels and faster ion saturation for two OMIEC matrices; (2) Excessive ion penetration disrupts molecular packing in the p(g2T-TT) film due to its glycol side chains, which potentially hinders efficient transport pathways and leads to a decline in device conductivity under high ion concentration electrolytes. As a result, the resistance of the n-type channel decreased from 7.87 ± 0.95 kΩ to 1.57 ± 0.40 kΩ as the electrolyte concentration increased from 1.0 mmol/L to 150 mmol/L PBS, while the resistance of the p-type channel exhibited a slight increase (Fig. 3c and Fig. S15 in Supporting information). Further increasing the ion concentration led to a rise in the resistance of both channels, indicating that 150 mmol/L PBS represents the optimal electrolyte concentration for balanced modulation of the p- and n-channels in the complementary inverter. At this concentration, both the p(g2T-TT) and N2200–2B films display synchronized electrochemical dynamics, redox kinetics, and doping behaviors, resulting in matched channel resistances. This ion-mediated symmetry in electronic behavior is critical for achieving high inverter performance (Fig. 3d). The synergistic regulation of redox rates, doping levels, and molecular ordering enables rapid switching transitions, directly contributing to enhanced voltage gain and superior signal transduction in the inverter circuit.

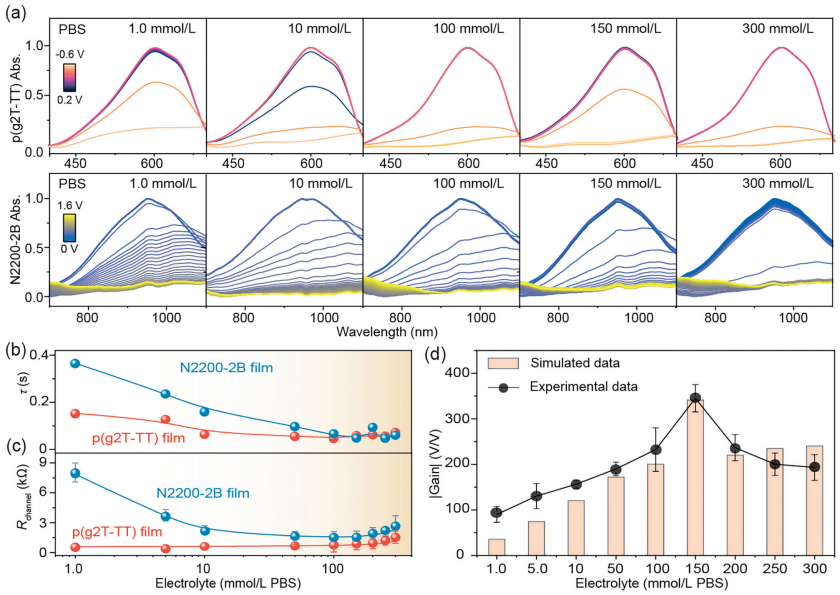


Fig. 3. (a) *In-situ* UV–vis absorption spectra of p(g2T-TT) and N2200–2B films doped in PBS electrolyte with varying ion concentrations. (b) Time constant (τ) for polaron formation in OMIEC films, and (c) channel resistance of the complementary inverter operated at V_{DS} of ±0.2 V. (d) Simulated and experimental gain values of the p(g2T-TT)/N2200–2B-based inverters as a function of electrolyte ion concentration.

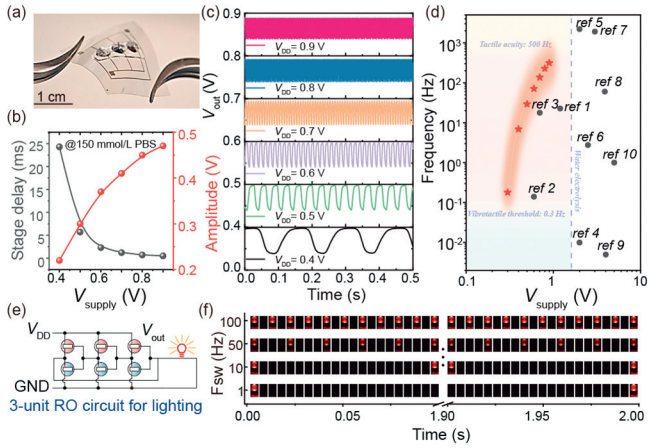


Fig. 4. (a) Photographs of a three-stage ring oscillator based on complementary OECT inverters fabricated on 25 μm polyimide substrate. (b) Stage delay and amplitude magnitude of a three-stage complementary ring oscillator at different supply voltages. The device can operate with supply voltages as low as 0.4 V and its signal propagation delays per stage as short as 0.53 ms. (c) The measured output waveform of the OECT-based complementary ring oscillator operates at a supply voltage ranging from 0.4 V to 0.9 V. All output voltages are confined within the range bounded by 0 V and the supply voltage V_{DD}. (d) Comparison of frequency in a state-of-the-art ring oscillator at a supply voltage below 5 V. Devices in the left middle region are desired for artificial nerve applications. (e) Circuit diagram of an LED switching driven by an OECT-based three-stage ring oscillator. (f) LED flickering in a consistent frequency of 1, 10, 50, and 100 Hz.

Efficient communication between artificial and biological nerves is often limited by frequency mismatches in signal transduction [5,16,32]. Here, we developed a three-stage ring oscillator integrated by the high-gain OECT-inverter operated under 150 mmol/L PBS (Fig. 4a). The oscillator began to operate at a low supply voltage $V_{DD} = 0.4$ V, with output frequencies increasing steadily as V_{DD} rose to 0.9 V (Figs. 4b and c). The lowest oscillating voltage and the highest output frequency are associated with electrolyte concentration (Fig. S16 in Supporting information). This behavior is governed by the oscillator frequency equation of $f = 1/(2Nt_p)$, where N is the number of stages and t_p is the propagation delay determined by the switching speed of the p- and n-type channels [33]. Fig. 4b summarizes the extracted propagation delays and amplitude magnitude. At $V_{DD} = 0.9$ V, the oscillator achieved a frequency of 294.4 ± 19.7 Hz with a stage delay of 0.53 ms. In contrast, at 0.4 V, the frequency dropped to 6.8 ± 0.2 Hz. As expected, increasing V_{DD} resulted in faster switching and higher output frequency (Fig. 4c). Remarkably, our device spans the broad frequency range of major human mechanoreceptors [16,32], approaching the resolution of human tactile acuity. It exhibits a wide and tunable frequency response under biologically safe voltages (<1 V), effectively covering the spectrum of human tactile sensing, including stimuli such as foot pressure [34,35]. It should be noted that previous reports have demonstrated oscillators operating above 100 Hz, but they typically required voltages exceeding 2 V, raising the high-power consumption and safety concerns for biointegration [34,36–38]. In contrast, our OECT-based oscillator combines broad frequency tunability with low-voltage operation, outperforming previously reported organic ring oscillators operated below 1 V (Fig. 4d and Table S2 in Supporting information), and has the potential to cover human tactile sensing transconductance frequency (Fig. S16 in Supporting information). To demonstrate functional stability, we constructed a logic circuit by coupling the oscillator with a commercial LED (Fig. 4e). Dynamic light switching was observed at 1, 10, 50, and 100 Hz, with a clear correlation between light pulses and oscillator frequency (Fig. 4f), confirming reliable output and strong potential for neuromorphic and sensory systems integration.

This study demonstrates that ion concentration–tuned matching of p(g2T-TT) and N2200–2B-based OECT inverters enables the construction of signal-transducing ring oscillators, offering a compatible interface for communication between electronic detectors and the nervous system. Initially, mechanoreceptors convert mechanical stimuli into electrical signals *via* opening ion channels such as Na^+/K^+ pump, Na^+ channel, and K^+ channel on the cell membrane [39,40], leading to an influx of ions and generating a localized change in membrane potential (Fig. 5a and Fig. S17 in Supporting information). To evaluate the potential application of OECT-based ring oscillators in neural-machine interfaces, we integrated the ring oscillator with a commercial pressure sensor (FSR20) to establish an artificial hybrid tactile neural pathway (Fig. S17 in Supporting information). This system was designed to

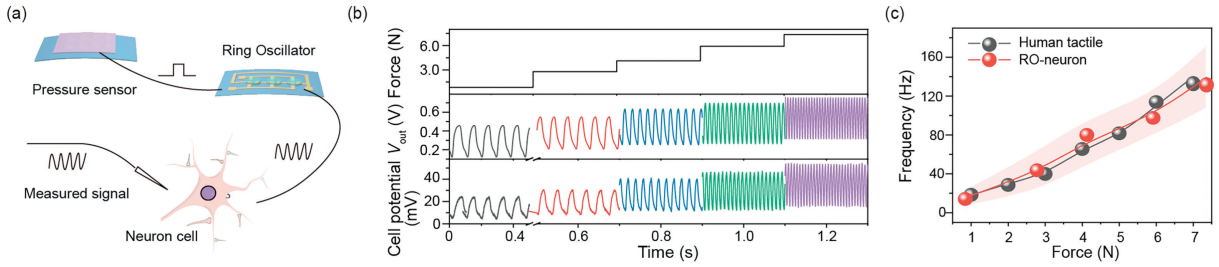


Fig. 5. (a) Setup of the electrical stimulation system for pressure-induced ring oscillator-dependent neuron stimulation. (b) The correlation plot among pressure force, frequency of the ring oscillator, and cell potential monitored in the circuit. Here, the RO generates voltage transitions in a waveform with fast rising and falling edges characteristic of square waves. (c) Comparison of the neuronal firing rate regulated by the ring oscillator with human tactile sensing frequency.

electrically stimulate HT22 mouse hippocampal neurons through frequency-encoded waveform signals [41], which is expected to trigger a synchronous neurophysiological electrical pulses [42,43]. To further demonstrate the bio-interfacing capability of our system, a commercial pressure sensor was integrated, and the OECT-based ring oscillator was employed in place of a conventional waveform generator to directly stimulate neurons. When mechanical forces were applied to the pressure sensor, corresponding digital pulse outputs were recorded by an Agilent DSO-X 3052A oscilloscope. Concurrently, real-time neuronal responses can be captured *via* whole-cell patch-clamp recordings (Fig. S18 in Supporting information), validating effective signal transduction from mechanical input to biological output, *via* the 3-RO circuit. Specifically, applied forces of 0.84, 2.8, 4.1, 5.9, and 7.4 N led to oscillator-driven voltage amplitudes ranging from 0.13 V to 0.75 V, which in turn elicited graded neuronal depolarizations from 24 mV to 53 mV (Fig. 5b). It should be noted that the convergence of both amplitude and temporal dynamics with canonical electrophysiological benchmarks indicates that the electrically stimulated membrane potential in our system accurately replicates physiological neural potentials (Fig. 5c). These results collectively demonstrate the functional fidelity and reliability of our experimental platform. Moreover, the firing frequency of the ring oscillator under each stimulus closely matched that of the evoked neuronal responses and exhibited a linear relationship with the applied pressure, indicating synchronized electrical signaling (Fig. S19 in Supporting information) [44]. Importantly, the oscillator operates below the water electrolysis threshold [38], enabling safe, biocompatible neuronal stimulation without the need for external amplification. These results underscore the potential of this low-voltage, ion-driven system for seamless mechanical-to-neural communication, demonstrating its ability to effectively mimic human mechanosensation and advance next-generation bioelectronic interfaces.

In summary, we present a high-performance complementary inverter whose switching behavior and gain are precisely regulated by an ion concentration–modulated balance between p-type and n-type channel conduction. This strategy enables fast electrical switching and overcomes the intrinsic limitations of traditional OECTs, such as sluggish ion transport and structural instability. By achieving an ultrahigh gain over 371 V/V at 0.7 V operation and constructing a 3-stage ring oscillator with 0.53 ms propagation delay, we enable frequency modulation across three orders of magnitude (0.1–312 Hz), directly matching human mechanoreceptor signaling spectra. When coupled with a commercial pressure sensor, the system successfully transduced mechanical stimuli into neuronal action potentials with synchronized frequency, emulating the function of biological tactile afferent nerves. Compared to conventional organic ring oscillators requiring >2 V operation, our ion-regulated architecture operates safely below 1 V while covering the biological tactile frequency ranges. This work demonstrates a scalable and biocompatible framework for ion-electron-coupled circuits, laying the foundation for next-generation neuromorphic electronics and neuron–machine interfaces. It should be noted that several real-world challenges must be addressed to ensure its reliable operation in the biological setting, such as noise sources that lower SNR and distort signals, instability from swelling and ion trapping that cause threshold voltage drift and gain variation, crosstalk between multiple channels, and biofouling or immune responses that degrade interfaces over time. Future efforts can be made in material engineering, circuit optimization, shielding, encapsulation, and surface modification, together with the fine-tuned electrolyte properties, to achieve stable, high-performance devices for well-designed neural–machine interfaces.

Declaration of competing interest

The authors declare that they have no known competing financial interests or personal relationships that could have appeared to influence the work reported in this paper.

CRediT authorship contribution statement

Xiangyuan Mei: Writing – review & editing, Writing – original draft, Methodology, Investigation. **Yu Xiao:** Writing – review & editing, Data curation. **Chaoyi Yan:** Writing – review & editing, Data curation. **Lingxuan Jia:** Writing – review & editing, Data curation. **Gang Song:** Writing – review & editing, Resources, Data curation. **Runjie Zhang:** Writing – review & editing, Data curation. **Weijie Wang:** Writing – review & editing, Data curation. **Fengting Lv:** Validation, Resources. **Xiaojuan Dai:** Writing – review & editing, Resources. **Liyao Liu:** Writing – review & editing, Validation, Data curation. **Ye Zou:** Validation, Resources. **Shu Wang:** Writing – review & editing, Resources. **Chong-an Di:** Writing – review & editing, Validation, Supervision, Funding acquisition, Conceptualization. **Daoben Zhu:** Visualization, Conceptualization. **Fengjiao Zhang:** Writing – review & editing, Writing – original draft, Conceptualization.

Acknowledgments

We acknowledge financial support from the National Natural Science Foundation (Nos. 22021002, 92477142), the Strategic Priority Research Program of the Chinese Academy of Sciences (No. XDB0520200), the Beijing Municipal Natural Science Foundation (No. Z220025) and Fundamental Research Funds for the Central Universities. We also thank Prof. Zhenjie Ni's group for supporting PNDI2TEG-2Tz materials.

Supplementary materials

Supplementary material associated with this article can be found, in the online version, at doi:10.1016/j.cclet.2025.112042.

References

[1] J. Rivnay, S. Inal, A. Salleo, et al., Nat. Rev. Mater. 3 (2018) 17086.
[2] D. Khodagholy, J. Rivnay, M. Sessolo, et al., Nat. Commun. 4 (2013) 2133.
[3] P. Gkoupidenis, Y. Zhang, H. Kleemann, et al., Nat. Rev. Mater. 9 (2024) 134–149.
[4] A. Saleh, A. Koklu, I. Uguz, et al., Nat. Rev. Bioeng. 2 (2024) 559–574.
[5] C. Zhao, J. Park, S.E. Root, et al., Nat. Rev. Bioeng. 2 (2024) 671–690.
[6] Y. Lee, Y. Liu, D.G. Seo, et al., Nat. Biomed. Eng. 7 (2023) 511–519.
[7] Y. Gao, J. Zhang, D. Liu, et al., Chin. Chem. Lett. 35 (2024) 108582.
[8] E.J. Fuller, S.T. Keene, A. Melianas, et al., Science 364 (2019) 570–574.
[9] P.C. Harikesh, C.Y. Yang, H.Y. Wu, et al., Nat. Mater. 22 (2023) 242–248.
[10] T. Sarkar, K. Lieberth, A. Pavlou, et al., Nat. Electron. 5 (2022) 774–783.
[11] Y. van de Burgt, A. Melianas, S.T. Keene, G. Malliaras, A. Salleo, Nat. Electron. 1 (2018) 386–397.
[12] Y. Zhao, W. Wang, Z. He, et al., Chin. Chem. Lett. 34 (2023) 108094.
[13] W. Huang, J. Chen, Y. Yao, et al., Nature 613 (2023) 496–502.
[14] I. Uguz, D. Ohayon, S. Yilmaz, et al., Sci. Adv. 10 (2024) eadi9710.
[15] H.Y. Wu, C.Y. Yang, Q. Li, et al., Adv. Mater. 34 (2022) 2106235.
[16] P. Delmas, J. Hao, L. Rodat-Despoix, Nat. Rev. Neurosci. 12 (2011) 139–153.
[17] D. Khodagholy, J.N. Gelinas, T. Thesen, et al., Nat. Neurosci. 18 (2015) 310–315.
[18] S. Chen, Z. Zhou, K. Hou, et al., Nat. Commun. 15 (2024) 7056.
[19] X. Liang, Y. Luo, Y. Pei, M. Wang, C. Liu, Nat. Electron. 5 (2022) 859–869.
[20] T. Leydecker, Z.M. Wang, F. Torricelli, E.J.C.S.R. Orgiu, Chem. Soc. Rev. 49 (2020) 7627–7670.
[21] C. Zhang, Y. Zheng, Y. Li, et al., Adv. Funct. Mater. 35 (2025) 2419706.
[22] P. Li, W. Sun, J. Li, et al., Science 384 (2024) 557–563.
[23] H.Y. Wu, J.D. Huang, S.Y. Jeong, et al., Mater. Horiz. 10 (2023) 4213–4223.
[24] M. Ma, L. Zhang, M. Huang, et al., Angew. Chem. Int. Ed. 64 (2025) e202424820.
[25] E. Stein, O. Nahor, M. Stolov, et al., Nat. Commun. 13 (2022) 5548.
[26] G.Y. Ge, J. Xu, X. Wang, et al., Nat. Commun. 16 (2025) 396.
[27] D.J. Wisniewski, L. Ma, O.J. Rauhala, et al., Nat. Commun. 16 (2025) 517.
[28] S. Wang, Y. Wang, X. Cai, et al., Nat. Electron. 8 (2025) 254–266.
[29] P. Romele, P. Gkoupidenis, D.A. Koutsouras, et al., Nat. Commun. 11 (2020) 3743.
[30] P. Romele, M. Ghittorelli, Z.M. Kovács-Vajna, F.J.N.c. Torricelli, Nat. Commun. 10 (2019) 3044.
[31] J. Liu, G. Ye, B.v.d. Zee, et al., Adv. Mater. 30 (2018) 1804290.
[32] E.B. Goldstein, Sensation and Perception, 5th ed., Cole Publishing Company, Brooks, 1999.
[33] J. Rabaey, A. Chandrakasan, B. Nikolic, Digital integrated circuits, A Design, 2nd, prentice Hall, Englewood Cliffs, NJ, 2002, pp. 33–34.
[34] B.C.K. Tee, A. Chortos, A. Berndt, et al., Science 350 (2015) 313–316.
[35] J.P. Vedel, J.P. Roll, Neurosci. Lett. 34 (1982) 289–294.
[36] Y. Kim, A. Chortos, W. Xu, et al., Science 360 (2018) 998–1003.
[37] W. Wang, Y. Jiang, D. Zhong, et al., Science 380 (2023) 735–742.
[38] H.D. Gesser, Applied Chemistry: A Textbook for Engineers and Technologists, Springer, 2002, pp. 162–163.
[39] D.C. Gadsby, Nat. Rev. Mol. Cell Biol. 10 (2009) 344–352.
[40] S. Choe, Nat. Rev. Neurosci. 3 (2002) 115–121.
[41] J. Liu, L. Li, W.Z. Suo, Life Sci. 84 (2009) 267–271.
[42] B.P. Bean, Nat. Rev. Neurosci. 8 (2007) 451–465.
[43] K. Malcolm, J. Casco-Rodriguez, arXiv:2303.10780, https://doi.org/10.48550/arXiv.2303.10780.
[44] D. Keppeler, R.M. Merino, D. Lopez, et al., EMBO J. 37 (2018) e99649.